ADVANCED ENERGY MATERIALS
www.advenergymat.de

Atomic Sn^{4+} Decorated into Vanadium Carbide MXene Interlayers for Superior Lithium Storage

Changda Wang, Shuangming Chen, Hui Xie, Shiqiang Wei, Chuanqiang Wu, and Li Song**

Ion intercalation is an important way to improve the energy storage performance of 2D materials. The dynamic energy storage process in such layered intercalations is important but still a challenge mainly due to the lack of effective operando methods. Herein, a unique atomic Sn^{4+}–decorated vanadium carbide (V_2C) MXene not only exhibiting highly enhanced lithium-ion battery (LIB) performance, but also possessing outstanding rate and cyclic stability because of the expanded interlayer space and the formation of V—O—Sn bonding is demonstrated. In combination with ex situ tests, an operando X-ray absorption fine structure measurement is developed to explore the dynamic mechanism of V_2C@Sn MXene electrodes in LIBs. The results clearly reveal the valence changes of vanadium (V), tin (Sn), and positive contribution of oxygen (O) atoms during the charging/discharging process, confirming their contribution for lithium storage capacity. The stability of intercalated MXene electrode is further in situ studied to prove the key role of V—O—Sn bonding.

2D materials[1] have attracted much attention, particularly in electrochemical energy storage fields.[2,3] Promoted by graphene's success,[4] MXenes (2D transition metal carbides/nitrides) are expected as one of most promising candidates for lithium-ion batteries (LIBs)[5] and capacitors,[6] because of the tunable chemical components and distinctive structural/electronic properties.[7] Among various MXenes, Ti_3C_2 and Ti_2C have been extensively studied.[8–10] For example, Ti_3C_2 MXenes delivered a capacity of 410 mA h g^{-1} for LIB in the initial study.[11] Interestingly, the capacity can be highly improved to around 800 mA h g^{-1} by intercalation with different cations such as NH^{4+}, Al^{3+}, and Sn^{4+}.[12–14] As comparison, V_2C MXene with small molecular weight can achieve much higher theoretical LIB capacity up to ≈940 mA h g^{-1}.[15] Unfortunately, the experimentally reported V_2C MXene only exhibited 260 mA h g^{-1} capacity under 1 C, which is far from the theoretical value.[16] Our recent work[17] has shown a 1100 mA h g^{-1} Li^+ storage capacity with good cyclic stability for V_2C MXene after cobalt ion intercalation. On the other side, although many works have been recently devoted to improving MXene's energy storage ability, rare operando studies are reported for probing the work mechanism during the charging and discharging process. Recently, in situ X-ray absorption fine structure (XAFS)[18,19] becomes an appropriate technique to study dynamic lithiation/delithiation mechanism. In particular, XAFS can determine dynamic valance change of metal atoms, as well as the real structural evolution of materials during the electrochemical reaction.[20]

Herein, we demonstrated, for the first time, the fabrication of Sn^{4+}-intercalated V_2C MXene (V_2C@Sn) through ion exchange process with outstanding specific capacity of 1284.6 mA h g^{-1} under 0.1 A g^{-1} so far. Notably, operando XAFS characterizations, combining with ex situ tests, were carefully performed to explore the dynamic lithiation/delithiation mechanism of V_2C@Sn MXene electrode. Our operando spectroscopic analysis clearly confirmed the electrochemical activity of Sn and V atoms, along with the positive contribution of O atoms and the hindrance of F atoms.

The schematic for fabricating Sn-intercalated V_2C MXene is shown in **Figure 1**a. V_2C@Sn MXene was obtained after the ion-exchange interaction between Sn^{4+} and the preintercalated K^+ in V_2C layers. The structure of each step is confirmed by the X-ray diffraction (XRD) patterns (Figure S1a, Supporting Information). The *c* lattice parameter (*c*-LP) of V_2C@Sn MXene is enlarged to 19 from 14.7 Å of V_2C MXene. Additionally, there is a little increase of (002) peak from V_2C–KOH to V_2C@Sn (Figure S1b, Supporting Information), indicating a decrease of interlayer spacing after Sn^{4+} intercalation. This change is mainly due to the stronger electrostatic interactions of Sn ion than K ion. The morphology of V_2AlC MAX (Figure 1b) is bulk with blocked multilayer, while V_2C MXene shows the typical accordion-like multilayer nanostructure (Figure 1c). However, V_2C@Sn MXene exhibits no obvious layer stripes (Figure 1d), and the signal intensity of Sn, as shown in Figure S2 (Supporting Information), is much stronger in the interlayer than other places, confirming that Sn^{4+} is mainly intercalated between V_2C MXene layers. High-resolution transmission electron microscopy (HRTEM) image in Figure 1e clearly

C. Wang, Dr. S. Chen, H. Xie, S. Wei, C. Wu, Prof. L. Song
National Synchrotron Radiation Laboratory
CAS Center for Excellence in Nanoscience
University of Science and Technology of China
Hefei, Anhui 230029, P. R. China
E-mail: csmp@ustc.edu.cn; song2012@ustc.edu.cn

The ORCID identification number(s) for the author(s) of this article can be found under https://doi.org/10.1002/aenm.201802977.

DOI: 10.1002/aenm.201802977

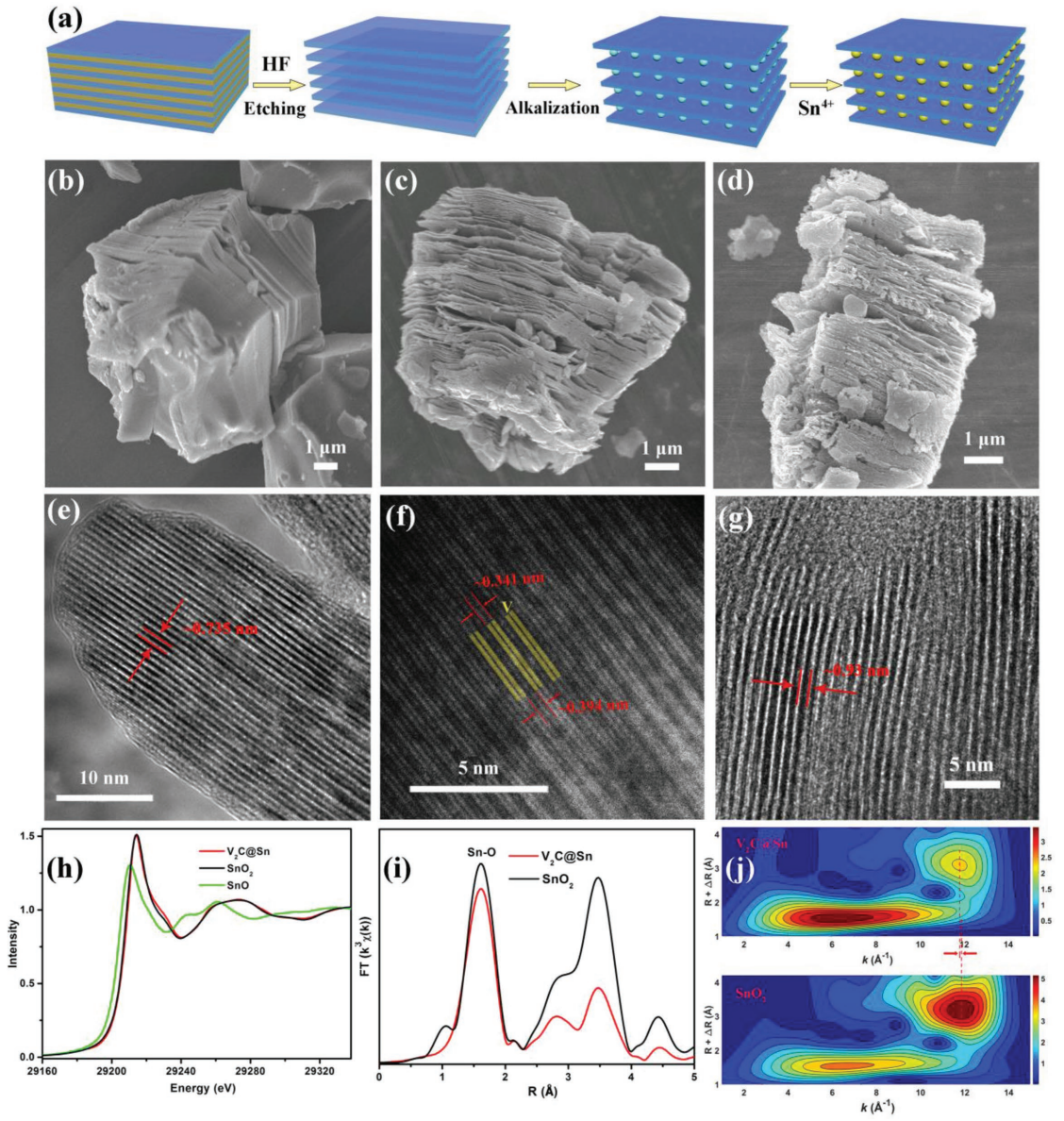

Figure 1. The fabrication process and morphology characterization of MXenes with static spectroscopic study. a) Schematic illustration of the fabrication process of Sn-intercalated V_2C MXene. b–d) SEM images of V_2AlC MAX, V_2C, and V_2C@Sn MXenes, respectively. e,f) HRTEM and STEM images of V_2C MXene. g) HRTEM of V_2C@Sn MXene. h) Normalized XANES spectra of Sn K-edge for V_2C@Sn MXene, SnO, and SnO_2 foil. i) Fourier transform spectra of Sn K-edge for V_2C@Sn MXene and SnO_2 foil from EXAFS. j) Wavelet transform (WT) of V_2C@Sn MXene and SnO_2, respectively.

reveals the interplanar spacing of V_2C MXene about 0.735 nm. The thickness of a single V_2C layer is measured to be about 0.341 nm (Figure 1f). And, the interlayer spacing between V_2C monolayers is about 0.394 nm which is several times larger than Li^+. The interplanar spacing of V_2C@Sn (Figure 1g) is then enlarged to 0.93 nm after Sn^{4+} decoration and cannot be stripped into monolayer dispersion through ultrasonic dissection methods. The amount of intercalated Sn is about 5.73 wt% and the content of K substantially decreases to about 0.5 wt% from over 3 wt% of V_2C–KOH according to plasma atomic emission spectrograph (Table S2, Supporting Information), indicating the successful of ion-exchange process. Static spectroscopic studies including X-ray photoelectron spectroscopy (XPS) and XAFS were performed to further explore the statement of Sn ions in V_2C MXene. High-resolution V 2p and O 1s XPS spectrum (Figure S3a, Supporting Information) shows three peaks at 517.3, 524.4, and 530.9 eV, revealing the existence of V—O bonding, similar to our former results.[17] High-resolution spectra of Sn $3d_{5/2}$ (Figure S3b, Supporting Information) shows the binding energy of 487.2 eV, which is 0.8 eV lower than the binding energy of Sn $3d_{5/2}$ for $SnCl_4 \cdot 5H_2O$ at 488.0 eV, indicating the combination of Sn^{4+} with V_2C MXene.[21] XAFS results (Figure 1h) show the same position of absorption edge for V_2C@Sn MXene and SnO_2, also indicating the successful intercalation of Sn^{4+}. The Fourier transform spectra of extended XAFS (FT-EXAFS) curves (Figure 1i)

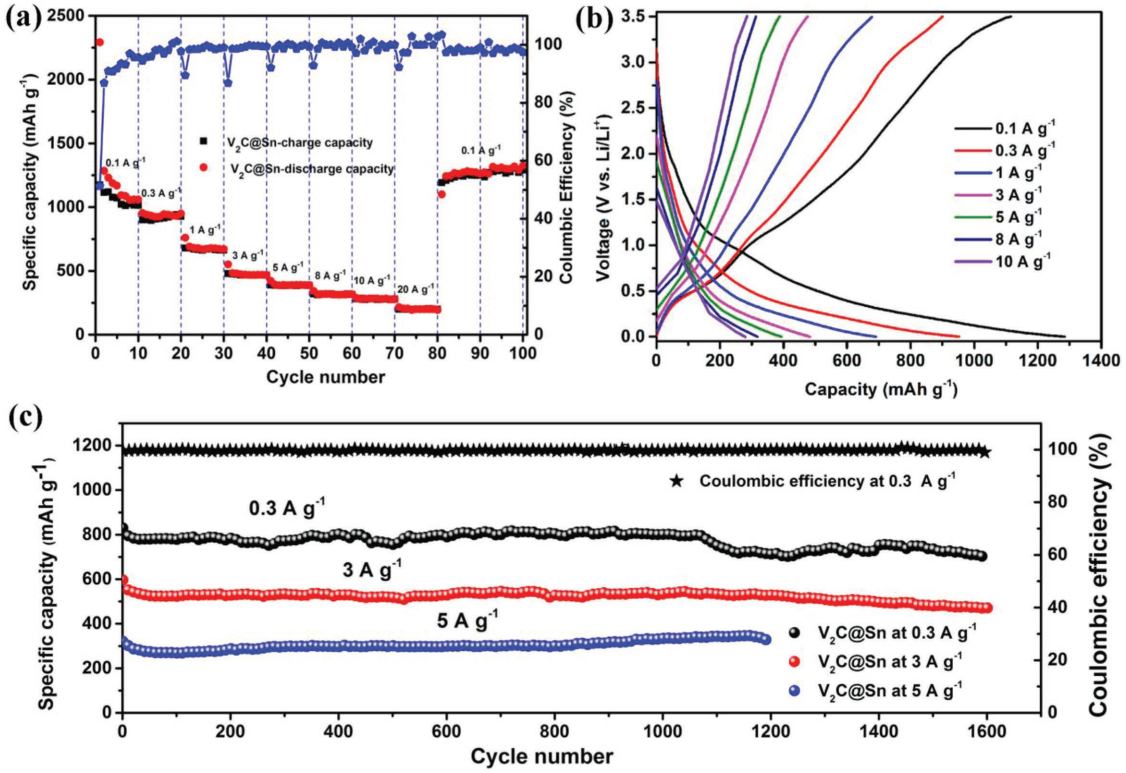

Figure 2. Electrochemical performance of V_2C@Sn MXene. a) Rate performance of V_2C@Sn MXene electrode. b) Galvanostatic charge and discharge curves cycled at different current densities. c) Long-term cycling performance and Coulombic efficiency of V_2C@Sn electrode under different current densities.

reveal the existence of Sn—O peak at about 1.6 Å together with the Sn—Sn peak at about 3.5 Å, which is confirmed from the best fitting results of SnO_2 and V_2C@Sn (Figure S4 and Table S1, Supporting Information). Wavelet transform (WT)[22] of Sn k-edge EXAFS oscillations (Figure 1j) shows the intensity maxima at 6.5 and around 12 $Å^{-1}$ of V_2C@Sn MXene and SnO_2, which associate with Sn—O and Sn—Sn contributions, respectively. The difference of Sn—Sn for V_2C@Sn MXene is ascribed to the interaction of Sn with V atoms. In conclusion, V—O—Sn covalent bonding is formed in V_2C@Sn MXene according to the analysis of XPS and XAFS results, which is expected to contribute on the lithium-ion storage according to our previous results.[23]

The electrochemical property of the as-prepared V_2C@Sn MXene electrode for LIB was evaluated by using CR2032 coin-type cells with lithium metal as the counter electrode and 1 M $LiPF_6$ as the electrolyte as shown in **Figure 2** and Figure S5 (Supporting Information). The estimated *b* value is around 0.5–0.6 for V_2C@Sn MXene electrode (Figure S5a, Supporting Information), indicating that the current is majorly semi-infinite linear diffusion controlled with a small part of surface-controlled. Therefore, this Sn-intercalated V_2C MXene electrode mainly shows lithium-ion battery behavior, which is quite different from the pristine V_2C MXene (pseudocapacitor).[17] After the first cycle of lithium and delithiated at 0.1 A g^{-1}, the Sn-intercalated MXene electrode can deliver a discharge capacity of 1284.6 mA h g^{-1} with a charge capacity of 1115.6 mA h g^{-1} (Figure 2a,b), which is much higher in comparison with pristine V_2C and cobalt ion–intercalated V_2C.[17] We believe that such differences are mainly due to the different mechanism of lithium storage. In addition, the Coulombic efficiency of V_2C@Sn electrode at the first cycle is 51.24%, which is due to the formation of solid electrolyte interface. With the increase of current densities from 0.3, 1, 3, 5, 8, 10 to 20 A g^{-1}, the stable and durable discharge capacity are various from 941, 690.8, 482.7, 393.2, 317.5, 279.7 to 205.2 mA h g^{-1} corresponding to the second cycle under related current densities. Moreover, the Coulombic efficiency is stable and higher than 96% even under high current densities, suggesting the excellent stability of V_2C@Sn electrode. Almost 100% reversible lithium storage capacity of 1262.9 mA h g^{-1} is still restored after 90 cycles when the current density returned to 0.1 A g^{-1}, implying marvelous rate performance. The electrochemical impedance spectroscopy (EIS) results (Figure S5b, Supporting Information) show the low equivalent series resistance of 5.2 Ω and charge transfer resistance of 39.8 Ω. It also reveals a short Warburg region and low relaxation time 2.6 s indicating the fast process of lithiation and delithiation with short transfer pathway due to the expanded interlayer spacing, confirming the fast charging and discharging ability. Notably, more than 90% capacity is remaining after 1600 cycles (Figure 2c) with Coulombic efficiency of nearly 100% under different current densities. Based on the above structural analysis and our previous work,[17] the outstanding rate performance and excellent cycling performance can be ascribed to rapid diffusion of Li^+ in the expanded interlayer and V—O—Sn bonding stabled V_2C structure during the charging/discharging processes.

To better understand the dynamic process and mechanism, ex situ XRD spectrum was first carried out on V_2C@Sn MXene

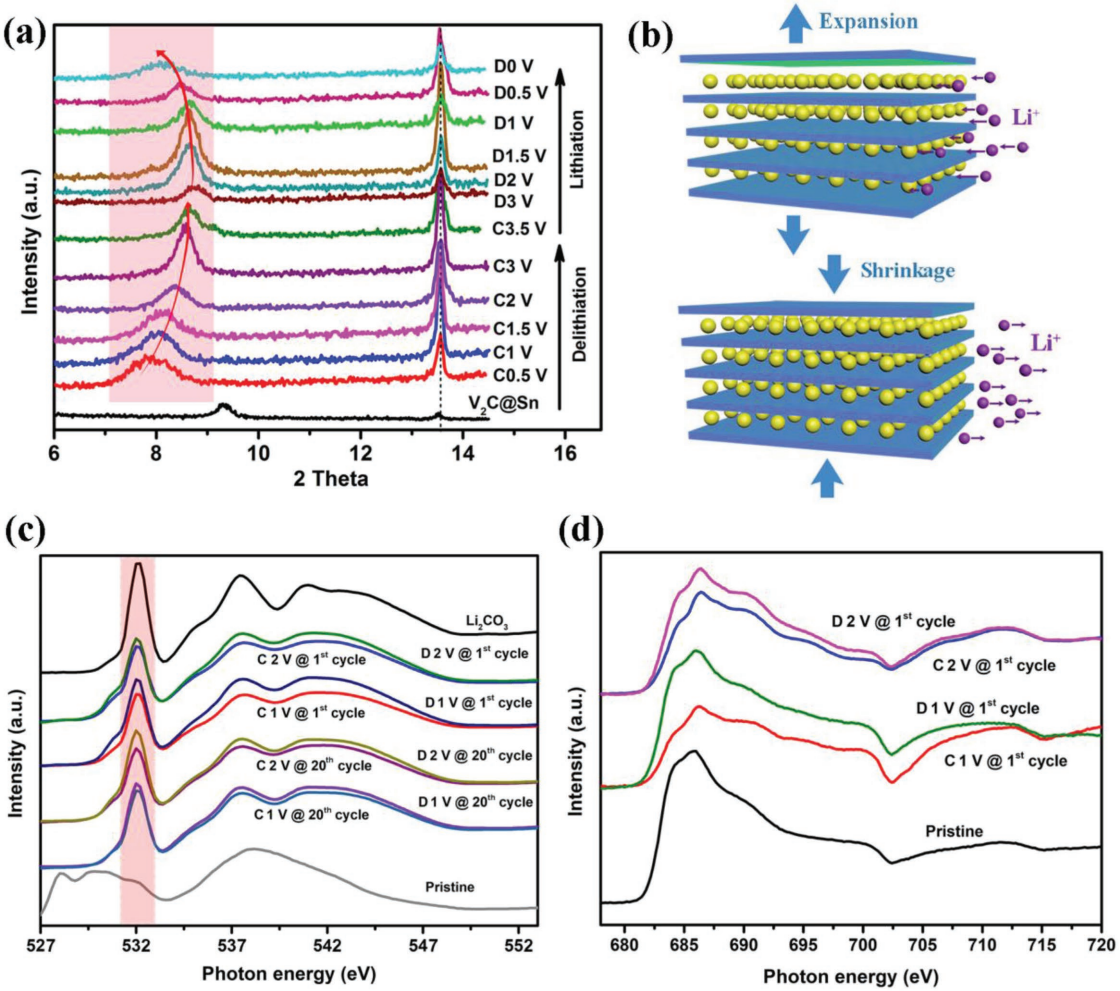

Figure 3. Ex situ spectrum study of V_2C@Sn electrode. a) XRD patterns of V_2C@Sn electrode during the charge and discharge processes. b) Schematic of the expansion and shrinkage for V_2C@Sn MXene during the lithiation and delithiation processes. c,d) O and F K-edge XAS spectra of V_2C@Sn electrode at different charge and discharge voltages, respectively.

electrode (**Figure 3**). During the discharging process from 3.5 V to 0 V (Figure 3a), the interlayer spacing increases due to the intercalation of Li^+ and then shrinkages during the delithiation process with the shifts evolution of (0002) peak (the schematic is shown in Figure 3b). This nearly reversible expansion and shrinkage strongly indicates the stable structure of V_2C@Sn MXene, which is beneficial to the high rate performance and long cycle stability. Moreover, the stable peak at 13.47° shows the electrochemical inactivity of V_2AlC MAX and the 0.7° decrease of (0002) peak at 3.5 V compared with the pristine sample ascribes to the incomplete delithiation and voltage delay. In fact, it is still unable to capture a deep view on the grading contributions of different atoms among V_2C@Sn electrode.

Subsequently, the study of O and F in V_2C@Sn MXene was further realized via ex situ X-ray absorption spectroscopy (XAS) spectra. In Figure 3c, the peak at 532.1 eV is the fingerprint feature of carbonate species like CO_3^{2-} which is the same with O K-edge of $LiCO_3$. The carbonate species could be related to the electrochemical reaction between oxygen on V_2C layers and the ethylene carbonate/dimethyl carbonate (EC/DMC) electrolyte which contributes to the lithium storage capacity. Furthermore, the intensity of carbonate groups shows a reversible and voltage-dependent evolution with little difference between the 1st cycle and the 20th cycle, indicating the stable state during charging/discharging. In addition, the unchanged shape of F K-edge (Figure 3d) suggests the electrochemical inactivity of fluorine. Therefore, future study may focus on less fluorine or fluorine-free MXenes in order to further enhance the LIB performance and explore their potential applications.[24,25]

As comparison with O and F atoms on the surface of V_2C@Sn, the hosting V and guesting Sn atoms are more important for LIB performance. Accordingly, operando Raman[26,27] (Figures S6 and S7, Supporting Information) and XAFS (**Figure 4**) measurements were carried out to investigate the structure evolution and electrochemical activity of vanadium and tin atoms in V_2C@Sn MXene. In situ Raman spectrum shows reversible evolution of the mode at 484 cm^{-1} which mainly comes from the collaborative vibrations of V and surface Sn-involving terminations.[28] This indicates the stable unit of V_2C@Sn MXene, and the stability during lithium storage process. Figure 4a

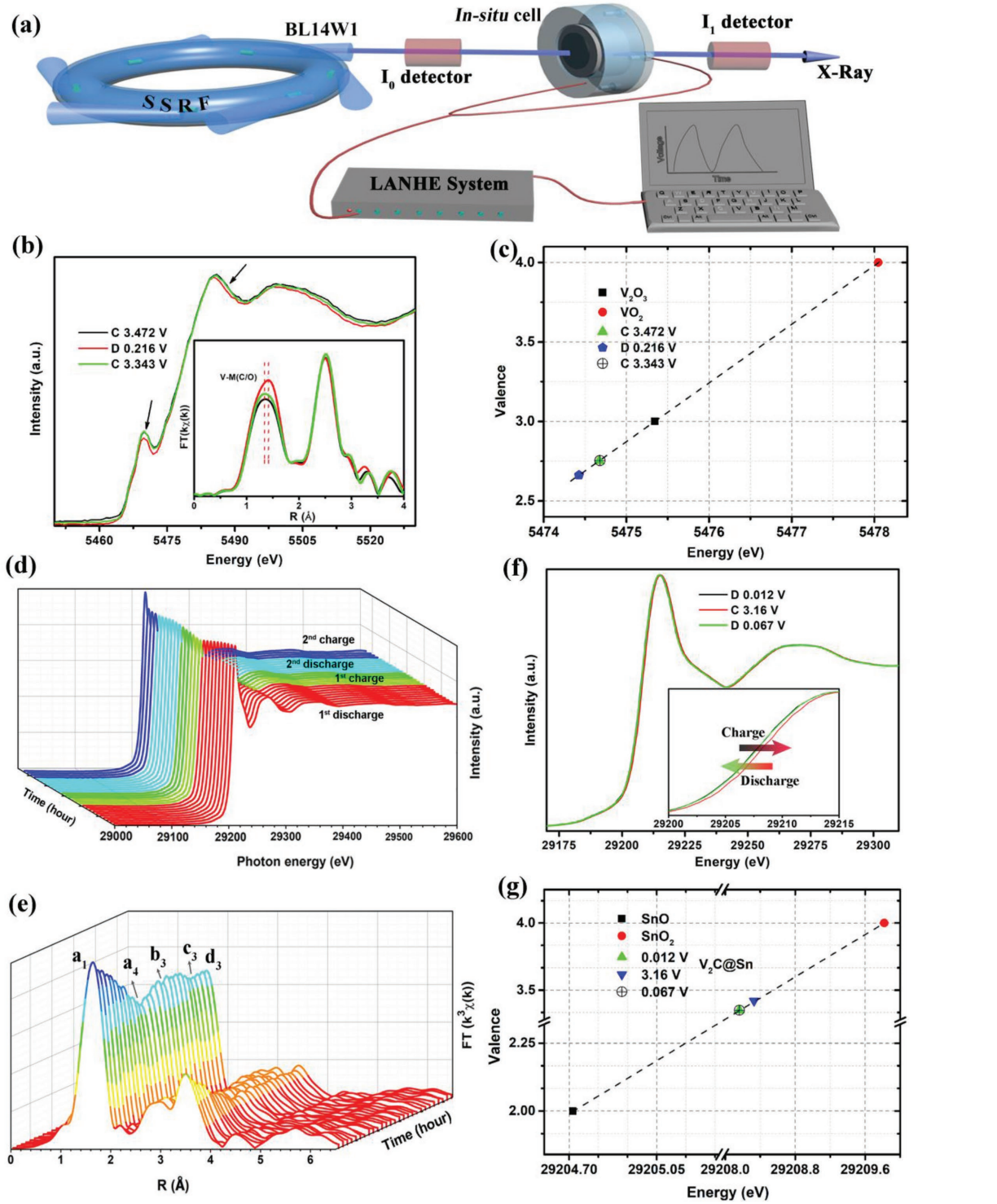

Figure 4. Operando V and Sn K-edge XAFS study for V_2C@Sn MXene electrode. a) Schematic diagram of the operando XAFS testing environment. b) Normalized XANES spectra of V K-edge at different voltages, inset: the corresponding Fourier-transformed V K-edge EXAFS spectra. c) Chemical valences of V atom in V_2O_3, VO_2, and V_2C@Sn electrode. d) In situ Sn K-edge XAFS spectra. e) Fourier-transformed Sn K-edge EXAFS spectra corresponding to (d). f) Normalized XANES spectra of Sn K-edge at different voltages, inset: enlargement of the absorption edge. g) Chemical valence of Sn atom in SnO, SnO_2, and V_2C@Sn electrode.

shows the schematic of in situ XAFS testing environment. The actual testing environment is shown in Figure S8 (Supporting Information). Figure 4b reveals the V K-edge XAFS spectra collected during the initial cycling process. With the decrease of voltage from charge (*C*) 3.472 V to discharge (*D*) 0.216 V, the absorption edge shifts to lower energy, and the bond length of

V—M (C/O) in the inset gets longer. Those changes attribute from the reduced valence of V which results from the intercalation of Li^+. When the voltage charges back to 3.343 V, both the absorption edge and bond length reversibly recover back due to the reoxidation of V, showing the stability of V_2C MXene. In addition, the highest valence of V at *D* 0.216 V is lower than +3 according to Figure S9 (Supporting Information). The range of valence fluctuation of V is then calculated to be +2.66 and +2.75 according to V_2O_3 and VO_2, as shown in Figure 4c.

As the most key atom, the in situ Sn K-edge spectra during the cycling under corresponding voltages (Figure S10, Supporting Information) was further collected to probe the changes of chemical state of Sn.[18] During the first discharge process from 3.5 to 0 V, the intensity of the main absorption peak for Sn K-edge (Figure 4d and Figure S11a (Supporting Information)) gradually decreases and the absorption edge shifts to lower energy which reflect a reduce of the average Sn oxidation state. Due to the intercalation of Li^+, it is clearly observed that the coordination number (Figure 4e and Figure S11b (Supporting Information)) of Sn also decreases. Afterward, they will gradually increase during the first charge process from b_1 to b_3, but the energy of absorption edge cannot reversibly recover back (Figure S11c,d, Supporting Information). This irreversibility contributes from the formation of solid electrolyte interphase (SEI) and the unstable interaction between Sn and Li during the initial process. In order to identify the average changes of Sn chemical valence, we recorded the data in stable charging–discharging processes after several cycles. The reversible shifts of absorption edges (Figure 4f) and bond length of Sn—O (Figure S12a, Supporting Information) for Sn K-edge indicate the stable oxidation-reduction evolution of intercalated Sn atoms, without any degradation. It can be seen from Figure S12b (Supporting Information) that the average valences of Sn at 0.012 and 3.16 V are in the range of +2—+4 by using SnO and SnO_2 as reference samples. As calculated, Figure 4g shows the average valence value changing from +3.35 to +3.42 with the voltage increasing from 0.012 to 3.16 V. More importantly, the valence change of Sn is reversible, further confirming its significant contribution to LIB capacity and stability.

In terms of above ex situ spectrum and operando measurements, we can conclude that the reversible chemical state changes of V, Sn, and the positive effect of O mainly contribute a great deal to the superior V_2C@Sn electrodes, thus achieving the highest Li^+ storage capacity and excellent stability to our knowledge.

In summary, Sn-intercalated V_2C MXene with enlarged *c*-LP of about 19 Å and formation of V—O—Sn bonding was designed and successfully synthesized. Combining with conventional characterizations, operando XAFS and Raman measurements were used to explore the mechanism of lithium storage. Our ex situ XRD results demonstrated the expansion and shrinkage of the V_2C interlayers during the lithiation/delithiation process. The O and F K-edge XAS spectrum showed the positive contribution of O atoms and hindrance of F atoms. More deeply, our operando XAFS of V, Sn K-edge and Raman characterizations clearly indicated the reversible electrochemical activity of Sn and V atoms, resulting in excellent LIB capacity and cycling ability. These results not only provide useful insight for better understanding the dynamic working process of MXenes-based electrodes, but also demonstrate the combination of ex situ and in situ spectroscopic techniques as appropriate meanings for future operando study.

Experimental Section

Synthesis of V_2AlC MAX: Powders of vanadium (99.5% metals basis, ≥325 mesh), Al (99.9% metals basis, 200–400 mesh), C (325 mesh) was first mixed in the ratio of 2:1.05:1, and ball-milled for 10 h at a speed of 400 rpm under Ar atmosphere. The mixture was then pressed into cylindrical shape under 10 MPa and heated in a corundum furnace to 1500 °C by 10 °C min^{-1} for 1 h under Ar atmosphere. After cooling to room temperature, V_2AlC MAX was obtained by grinding the bulk to 800 mesh powder.

Synthesis of V_2C@Sn: Briefly, Al layer was etched from V_2AlC MAX by concentrated HF at 35 °C for 5 days. To prepare Sn-intercalated V_2C MXene, V_2C powder was first alkalized by immersing in 2 M KOH at 40 °C for 1 day; then, transferred into 0.2 M stannic chloride at 40 °C for another 2 days. V_2C@Sn powder was finally obtained after washing and freeze-drying.

The Preparation of V_2C@Sn Electrodes for XRD and O, F K-Edge XAFS Characterization at Different Voltages: The samples were prepared by dismantling the coin batteries and washing the electrolyte and other by-product away by dimethyl carbonate in Ar-filled glove box after the batteries were stopped at different charging and discharging voltages. The electrodes were tested directly for XRD and XAFS to show the changes of (0002) peak and the changes of O, F K-edge spectra.

Electrochemical Measurements: The working electrodes were composed of active materials, carbon black, and polyvinylidene fluoride (PVDF) powder at mass ratio of 7:2:1. It was coated on a copper substrate after uniformly grinding in N-methyl pyrrolidone (NMP) and dried in vacuum oven under 100 °C. The electrode was assembled into coin-type cell with Li as the counter electrode and 1 M $LiPF_6$ in EC/DMC (1:1) as electrolyte. The assembling process was conducted in an argon-filled glove box (MBraun, Germany). Rate capability and cyclability were achieved on a Land CT2001A cell test system at room temperature in the range of 0–3.5 V. Meanwhile, cyclic voltammetry (CV) at various scan rates in the voltage range of 0–3.5 V and EIS testing were performed using a CHI660D electrochemical workstation.

Material Characterization: Scanning electron microscope (SEM) was carried out with a field emission SEM (15 kV, JEOL, JSM-6700F). TEM images, HRTEM images, and elemental mapping images were obtained by a transmission electron microscope (JEOL JEM2010). High-angle annular dark field-scanning transmission electron microscopy (HAADF-STEM) was observed on a JEOL JEM-ARF200F electron microscope (200 kV) with a spherical aberration corrector. XRD patterns were recorded on a D8-Advance power diffract meter equipped with Cu Kα radiation (λ = 1.54178Å). The element contents were obtained by plasma atomic emission spectrograph (Optima 7300 DV). XPS results were get from electron energy disperse spectroscopy (ESCALAB 250). In situ Raman results were collected on Horiba XploRA Raman system with a 532 nm Ar laser. Before the uniformly grinded samples were coated on a copper substrate, the copper substrate was created many small holes manually via a pin. Then, the pin-holed V_2C@Sn electrode was directly put into the in situ cell (Beijing Scistar Technology Co., Ltd.) with Li foil as the counter electrode and 1 M $LiPF_6$ in EC/DMC (1:1) as electrolyte. The Raman spectra was collected during the charging and discharging processes which were controlled by LANHE system.

The Sn K-edge XAFS measurements were made in the transmission mode at the beamline 14W1 in Shanghai Synchrotron Radiation Facility (SSRF). The X-ray was monochromatized by a double-crystal Si(311) monochromator, and the energy was calibrated using a Sn metal foil for Sn K-edge. XAFS data were analyzed with the WinXAS3.1 program.[29] Theoretical amplitudes and phase-shift functions of Sn—O were calculated with the FEFF8.2 code[30] using the crystal structural parameters of the SnO_2. The operando V and Sn K-edge XAFS measurements were also achieved at beamline 14W1 in SSRF,

respectively. The moderate V_2C@Sn sample was mixed with carbon black and rolled into a wafer with the diameter of 10 mm. This wafer was directly put into the in situ cell (Beijing Scistar Technology Co., Ltd.) with Li foil as the counter electrode and 1 M $LiPF_6$ in EC/DMC (1:1) as electrolyte. The XAFS spectra were collected during the charge and discharge processes which were controlled by LANHE system. The O, F K-edge X-ray absorption near edge structure (XANES) measurements of V_2C@Sn electrodes were performed at the beamline BL12B-a (CMD) in Hefei Synchrotron Radiation Facility, National Synchrotron Radiation Laboratory (NSRL).

Supporting Information

Supporting Information is available from the Wiley Online Library or from the author.

Acknowledgements

This work was financially supported by National Key R&D Program of China (2017YFA0303500), the NSFC (U1532112, 11574280, 11605201, 21727801), the Fundamental Research Funds for the Central Universities (WK2310000074), the Anhui Provincial Natural Science Foundation (1708085QB27), the CAS Key Research Program of Frontier Sciences (QYZDB-SSW-SLH018), and the CAS Interdisciplinary Innovation Team. L.S. acknowledges the Key Laboratory of Advanced Energy Materials Chemistry (Ministry of Education) Nankai University (111 project, B12015). The authors thank the Shanghai synchrotron Radiation Facility (14W1 endstation, SSRF), the Hefei Synchrotron Radiation Facility (Photoemission and MCD Endstations, NSRL), and the USTC Center for Micro and Nanoscale Research and Fabrication for helps in characterizations. The authors also thank Dr. Biao Li from the College of Engineering, Peking University for the help in in situ XRD measurement.

Conflict of Interest

The authors declare no conflict of interest.

Keywords

atomic ion intercalation, ex situ study, layered materials, Li-ion storage, operando spectroscopic study

Received: September 25, 2018
Revised: November 12, 2018
Published online:

[1] C. Tan, Z. Lai, H. Zhang, *Adv. Mater.* **2017**, *29*, 1701392.
[2] H. Tang, Q. Hu, M. Zheng, Y. Chi, X. Qin, H. Pang, Q. Xu, *Prog. Nat. Sci-Mater* **2018**, *28*, 133.
[3] Q. Yun, Q. Lu, X. Zhang, C. Tan, H. Zhang, *Angew. Chem., Int. Ed.* **2018**, *57*, 626.
[4] Y. Zhu, S. Murali, M. D. Stoller, K. J. Ganesh, W. Cai, P. J. Ferreira, A. Pirkle, R. M. Wallace, K. A. Cychosz, M. Thommes, D. Su, E. A. Stach, R. S. Ruoff, *Science* **2011**, *332*, 1537.
[5] Q. Tang, Z. Zhou, P. Shen, *J. Am. Chem. Soc.* **2012**, *134*, 16909.
[6] M. Ghidiu, M. R. Lukatskaya, M. Q. Zhao, Y. Gogotsi, M. W. Barsoum, *Nature* **2014**, *516*, 78.
[7] B. Anasori, M. R. Lukatskaya, Y. Gogotsi, *Nat. Rev. Mater.* **2017**, *2*, 16098.
[8] D. Xiong, X. Li, Z. Bai, S. Lu, *Small* **2018**, *14*, 1703419.
[9] M. Naguib, J. Come, B. Dyatkin, V. Presser, P.-L. Taberna, P. Simon, M. W. Barsoum, Y. Gogotsi, *Electrochem. Commun.* **2012**, *16*, 61.
[10] C. Zeng, F. Xie, X. Yang, M. Jaroniec, L. Zhang, S. Z. Qiao, *Angew. Chem., Int. Ed.* **2018**, *57*, 8540.
[11] O. Mashtalir, M. Naguib, V. N. Mochalin, Y. Dall'Agnese, M. Heon, M. W. Barsoum, Y. Gogotsi, *Nat. Commun.* **2013**, *4*, 1716.
[12] M. R. Lukatskaya, O. Mashtalir, C. E. Ren, Y. Dall'Agnese, P. Rozier, P. L. Taberna, M. Naguib, P. Simon, M. W. Barsoum, Y. Gogotsi, *Science* **2013**, *341*, 1502.
[13] C. E. Ren, M. Q. Zhao, T. Makaryan, J. Halim, M. Boota, S. Kota, B. Anasori, M. W. Barsoum, Y. Gogotsi, *ChemElectroChem* **2016**, *3*, 689.
[14] X. Wu, Z. Wang, M. Yu, L. Xiu, J. Qiu, *Adv. Mater.* **2017**, *29*, 1607017.
[15] J. Hu, B. Xu, C. Ouyang, S. A. Yang, Y. Yao, *J. Phys. Chem. C* **2014**, *118*, 24274.
[16] M. Naguib, J. Halim, J. Lu, K. M. Cook, L. Hultman, Y. Gogotsi, M. W. Barsoum, *J. Am. Chem. Soc.* **2013**, *135*, 15966.
[17] C. Wang, H. Xie, S. Chen, B. Ge, D. Liu, C. Wu, W. Xu, W. Chu, G. Babu, P. M. Ajayan, L. Song, *Adv. Mater.* **2018**, *30*, 1802525.
[18] L. Zhang, D. Sun, J. Kang, H. T. Wang, S. H. Hsieh, W. F. Pong, H. A. Bechtel, J. Feng, L. W. Wang, E. J. Cairns, J. Guo, *Nano Lett.* **2018**, *18*, 4506.
[19] T. Nedoseykina, M. G. Kim, S. A. Park, H. S. Kim, S. B. Kim, J. Cho, Y. Lee, *Electrochim. Acta* **2010**, *55*, 8876.
[20] M. R. Lukatskaya, S. M. Bak, X. Q. Yu, X. Q. Yang, M. W. Barsoum, Y. Gogotsi, *Adv. Energy Mater.* **2015**, *5*, 1500589.
[21] J. Luo, X. Tao, J. Zhang, Y. Xia, H. Huang, L. Zhang, Y. Gan, C. Liang, W. Zhang, *ACS Nano* **2016**, *10*, 2491.
[22] T. He, S. Chen, B. Ni, Y. Gong, Z. Wu, L. Song, L. Gu, W. Hu, X. Wang, *Angew. Chem., Int. Ed.* **2018**, *57*, 3493.
[23] C. Wu, H. Xie, D. Li, D. Liu, S. Ding, S. Tao, H. Chen, Q. Liu, S. Chen, W. Chu, B. Zhang, L. Song, *J. Phys. Chem. Lett.* **2018**, *9*, 817.
[24] O. Mashtalir, M. R. Lukatskaya, A. I. Kolesnikov, E. Raymundo-Pinero, M. Naguib, M. W. Barsoum, Y. Gogotsi, *Nanoscale* **2016**, *8*, 9128.
[25] Y. Wen, T. E. Rufford, X. Chen, N. Li, M. Lyu, L. Dai, L. Wang, *Nano Energy* **2017**, *38*, 368.
[26] K. Wang, N. Wang, J. He, Z. Yang, X. Shen, C. Huang, *ACS Appl. Mater. Interfaces* **2017**, *9*, 40604.
[27] M. Hu, Z. Li, T. Hu, S. Zhu, C. Zhang, X. Wang, *ACS Nano* **2016**, *10*, 11344.
[28] A. Champagne, L. Shi, T. Ouisse, B. Hackens, J. C. Charlier, *Phys. Rev. B* **2018**, *97*, 115439.
[29] T. Ressler, *J. Synchrotron Radiat.* **1998**, *5*, 118.
[30] A. L. Ankudinov, B. Ravel, J. J. Rehr, S. D. Conradson, *Phys. Rev. B* **1998**, *58*, 7565.